Applied Mathematics for Modern Challenges
Vol. 4, 2025, pp. 1-16
doi:10.3934/ammc.2025006

REDUCING THE SAMPLING BURDEN OF FOURIER SENSING WITH A NON-RECTANGULAR FIELD-OF-VIEW

Nicholas Dwork*[1], Erin K. Englund[2] and Alex J. Barker[2]

[1]Department of Biomedical Informatics,
University of Colorado — Anschutz Medical Center, USA

[2]Department of Radiology, University of Colorado — Anschutz Medical Center, USA

(Communicated by Fernando Guevara Vasquez)

Abstract. Fourier sensing devices collect data in the frequency domain. For example, Magnetic Resonance Imaging (MRI) is a Fourier sensing modality where the user has the freedom to choose which spatial frequencies are sampled. With Fourier sensing, it is commonly the case that the field-of-view (FOV), the area of space to be imaged, is known prior to reconstruction. Most commonly, reconstruction algorithms have focused on FOVs with simple geometries. This leads to sampling patterns that are more burdensome (with more samples) than necessary. Due to the reduced area of imaging possible with an arbitrary (e.g., non-rectangular and non-convex) FOV, the number of samples required for a high-quality image is reduced. However, when an arbitrary FOV has been considered, the reconstruction algorithm has been computationally expensive. In this manuscript, we present a method to reduce the sampling burden for an arbitrary FOV with an accompanying direct (non-iterative) and computationally efficient reconstruction algorithm. We also present a method to decrease the computational cost of the iterative POCSENSE algorithm used with a non-rectangular FOV. We present results using MRI data of an ankle, a pineapple, and a brain.

1. Introduction.

Fourier sensing imaging devices collect data in the frequency domain; some form of inverse Fourier transform is then required to reconstruct the image. Examples of Fourier sensing systems include Magnetic Resonance Imaging (MRI), Computed Tomography, Optical Coherence Tomography, Synthetic Aperture Radar, and Radio Astronomy. For these modalities, it is commonly the case that the field-of-view (FOV), the area of space to be imaged, is rectangular. Assuming the sampling pattern is a Cartesian grid, this rectangular FOV dictates the spacing between samples required to satisfy the Nyquist-Shannon sampling theorem: the spacing between grid points in the frequency domain is the inverse size of the FOV in the corresponding dimension [33]. This sampling pattern is commonly referred to as *fully-sampled* [3, 13, 25, 46].

Past works have attempted to develop reconstruction algorithms that are able to generate high-quality images from fewer samples with a reduced non-rectangular FOV [1, 12, 27, 30, 39]. An FOV of this type could better isolate empty space

---

2020 *Mathematics Subject Classification.* Primary: 94A12; Secondary: 41A05.

Key words and phrases. Fourier sensing, support, magnetic resonance imaging, reconstruction, sampling.

*Corresponding author: Nicholas Dwork.

from the object to be imaged (Fig. 1). We will separate these methods into two types: *direct* methods and *iterative* methods. For example, in the special case of a hexagonal FOV, one can sample with a hexagonal sampling pattern and use the inverse hexagonal Fast Fourier Transform (HexFFT) to reconstruct the image [19, 9]. The HexFFT can be implemented with standard and computationally efficient FFT implementations [7]. Though useful, the HexFFT is restricted to hexagonal FOVs. Moreover, the pixels in the image domain are hexagons, which is non-standard for current displays. Other works have proposed using a circular or elliptical FOV in combination with an angular sampling pattern (e.g., radial, spiral, or PROPELLER) [45, 27]. Still other methods do generate a sampling pattern in accordance with a more general, but still convex, FOV [1, 12, 30]. These methods use a lattice as the sampling pattern to take advantage of a non-rectangular FOV [1]. The lattice used is specific to the support of the object imaged (i.e., the region of the field of view where sample is present). Note that a hexagonal sampling pattern is a special case of a lattice; so these methods can be thought of generalizations of the hexagonal sampling pattern. With these methods, the lattice sampling pattern in combination with the reconstruction method limits the field of view (FOV) to convex shapes. In this manuscript, we present a sampling pattern and a direct reconstruction method that accommodates a non-convex FOV and generates an image with square pixels.

Several iterative methods exist that accommodate a more general FOV [36, 48, 28, 43, 38, 23]. In [36], Papoulis presents an iterative method based on a known support. In [48], Wang et al. extend this technique to also estimate the support during the iterative reconstruction process. In [43], Samsanov et al. describe POCSENSE, a method for taking advantage of an arbitrary FOV similar to that of [36] for the parallel MRI setting (where multiple sensing coils simultaneously collect data of the object) that also accommodates additional constraints. These methods do not specify a sampling pattern and they reconstruct the entire rectangular FOV with the assumption that the values of pixels outside the support be 0. Other methods assume that the support is a subset of the FOV but not known prior to image reconstruction (e.g., [23]). In this manuscript, we assume that the FOV is known and that the support is a subset of this FOV.

We present a direct (non-iterative) method for reconstructing an image from a reduced sampling pattern generated from a non-rectangular FOV[1]. We show examples where high-quality images are reconstructed from a reduced sampling pattern using MRI data of an ankle, a pineapple, and a brain. We extend this technique to reconstruct high-quality images from parallel MRI data, where multiple coils (i.e., antennas) simultaneously image the object. We also present an iterative method for parallel MRI that accommodates an arbitrary FOV and is more efficient than POCSENSE. Finally, we present several avenues for future work.

2. Background.

For the purposes of discussion, we assume that the non-rectangular FOV is closed, compact, and that it is known *a priori*. Furthermore, we assume that the support of the object to be imaged is a subset of this FOV. With MRI, the FOV is commonly determined from a *localizer*, a low-quality image generated from data collected with a fast scan used for the purposes of identifying the relevant anatomy and selecting the FOV. Currently, the procedure for clinical MRI

---

[1] Note that an early version of this work was presented at the 2024 IEEE conference on Computational Imaging and Synthetic Apertures.

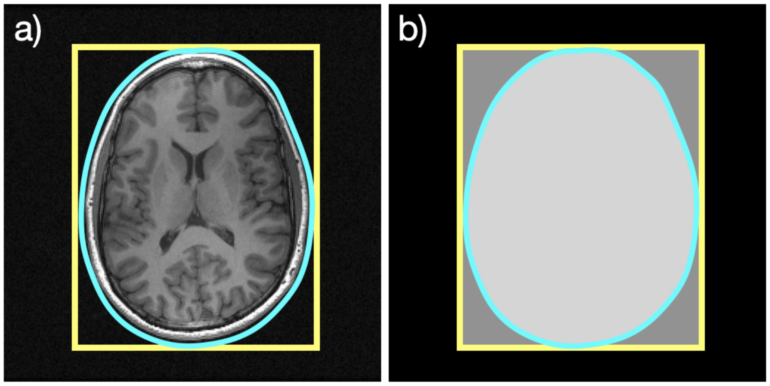

Figure 1. An axial slice of a brain: a) the yellow rectangle and the cyan contour represent a rectangular and non-rectangular FOV, respectively, and b) a depiction of the reduced area in the non-rectangular FOV.

is for the technologist to select a rectangle on the localizer image that is used as the FOV. Instead, the technologist could draw an arbitrary contour (or a set of contours, if the object to be imaged is not connected - e.g., two legs) that would be the non-rectangular FOV. With radio astronomy, it may be known that the object of interest only encompasses a non-rectangular volume of space from past imaging [8]. With optical coherence tomography, the FOV is specified by the arc subtended by the laser beam [49].

The two-dimensional (2D) Fourier transform of a function $I : \mathbb{R}^2 \to \mathbb{C}$ is

$$\mathcal{F}\{I\}\,(k_u, k_v) = \int_{-\infty}^{\infty} \int_{-\infty}^{\infty} I(u,v) e^{-i2\pi(k_u u + k_v v)}\, du\, dv. \tag{1}$$

With Fourier sensing devices, values of $\mathcal{F}\{I\}$ are recorded for a set of individual spatial frequency coordinates (k_u, k_v). With MRI, values of $\mathcal{F}\{\sigma I\}$ are measured, where $\sigma : \mathbb{R}^2 \to \mathbb{C}$ quantifies the sensitivity of the antenna as a function of space. Parallel MRI simultaneously collects data with multiple antennas.

To satisfy the Nyquist-Shannon sampling theorem with a FOV of dimensions $\text{FOV}_u \times \text{FOV}_v$, the sampling pattern is a Cartesian grid centered on the $(0,0)$ frequency and the spacing between samples should be less than $1/\text{FOV}_u$ and $1/\text{FOV}_v$ in the u and v dimensions, respectively. The resolution of the resulting image is determined by the number of samples. Such a sampling pattern for the arbitrary object of Fig. 2a is depicted in Fig. 2b.

The insight that leads to the method of this manuscript is that any non-rectangular image can be decomposed into the sum of two images with smaller supports. For example, the object of Fig. 2a can be decomposed as shown in Fig. 3b-c. As long as we are careful about how we separate the image into its parts, the sampling pattern required to satisfy the Nyquist theorem for the image's components has fewer samples than the fully-sampled pattern represented in Fig. 2b.

3. **Methods.** In this section, we will first discuss how the reduced sampling pattern is generated. We will then present a method for reconstructing the image from the reduced sampling pattern.

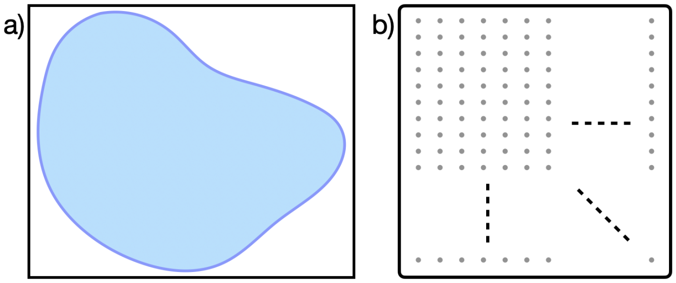

Figure 2. A depiction of a non-rectangular FOV and its sampling pattern. The dark blue contour in (a) shows the boundary of the non-rectangular FOV, and (b) shows the full sampling pattern associated with a rectangular FOV.

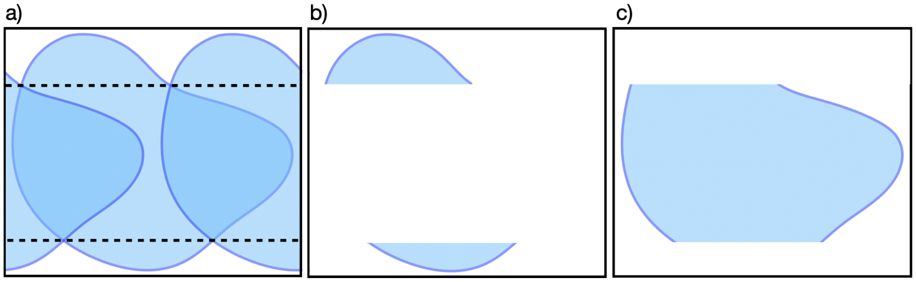

Figure 3. A depiction of how a non-rectangular FOV is separated into components: a) shows an aliased version non-rectangular FOV of Fig. 2a where the dashed lines separate the outer region of (b) and the inner region of (c).

3.1. **Generating the sampling pattern.** Consider the reconstruction created by applying the inverse Discrete Fourier Transform (DFT) to a sampling pattern that consists only the even columns of the full sampling pattern (where the odd columns are filled with 0 values). The reconstructed image includes significant aliasing; it is the sum of the image with itself circularly shifted by half the rectangular FOV, as shown in Fig. 3a. For the example depicted, the boundary of the original object intersects that of its aliased copy in four places. The dashed horizontal lines cross these intersection points. Let us denote the region consisting of that above the top dashed line as well as that below the bottom dashed line – as the outer region (Fig. 3b), and the remaining areas – the region within the two dashed lines – as the inner region (Fig. 3c). The sampling pattern for the non-rectangular FOV was created by combining even columns for a fully-sampled pattern (Fig. 4a) with the odd columns for a sampling pattern for an FOV with a reduced vertical extent (Fig. 4b).

The inner and outer regions can be identified as follows. Let S be a 2D array, the size of the desired image, that indicates the support based on the non-rectangular FOV. That is, those elements of S that correspond to pixels within the FOV have values of 1, and all other elements have values of 0. The rows of S in the inner region are identified by identifying those rows of $S + \tau_u(FOV_u/2)$ with any element equal to 2; here, $\tau_u(\cdot)$ represents a circular shift in the horizontal (or u) dimension. The rows of S in the outer region are the complement set of those in the inner

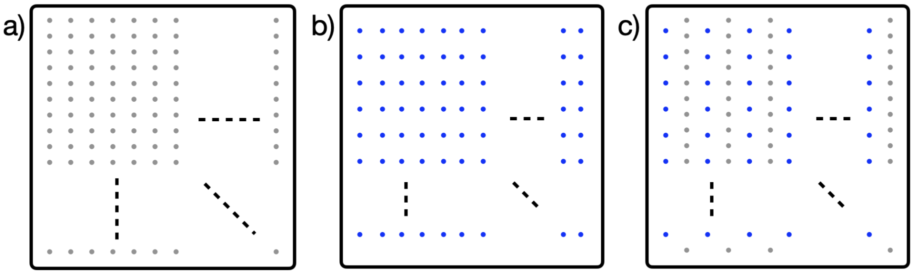

Figure 4. Sampling patterns related to the FOV: a) the full sampling pattern based on the rectangular FOV, b) the full sampling pattern for the inner region, and c) the proposed sampling pattern for the non-rectangular FOV.

region. After the rows of the inner region are identified, the support of the inner region S_{inner} is found by intersecting the inner region with the non-rectangular FOV and its interior. Performing the same procedure with the rows of the outer region yields the support of that region S_{outer}.

The aliased image of Fig. 3a can be reconstructed by performing an inverse DFT on the even columns of the full sampling pattern with those values of the odd columns set to 0 (Fig. 2b). Note that, in the aliased image (Fig. 3a), the outer region does not overlap itself. Performing a Hadarmard product (i.e., a point-wise product, denoted by $\odot$) between the aliased image and S_{outer} (Fig. 3a) yields an uncorrupted image of the outer region (Fig. 3b). This shows that we can accurately reconstruct the outer region using every other column of the full sampling pattern.

Thus far, our sampling pattern consists of samples only from the even columns of the full sampling pattern. We will now add additional samples into the sampling pattern to reconstruct the inner image depicted in Fig. 3c.

If we were going to create a full sampling pattern for the inner region, we would create a Cartesian grid with a horizontal spacing equal to that depicted in Fig. 2b, since the horizontal extent of the inner region is the same as that of the full non-rectangular FOV. However, the vertical extent of the inner region is smaller than that of the non-rectangular FOV; thus, its samples could be separated further apart vertically. The full sampling pattern would be a Cartesian grid with points separated horizontally by an amount less than $1/\text{FOV}_u$ but with points separated vertically by an amount less than $1/\text{FOV}_{v,\text{inner}}$; this is depicted in Fig. 4b. This Cartesian grid satisfies the Nyquist-Shannon sampling theorem. Therefore, any pattern with a density of samples higher than that of this grid also satisfies the Nyquist-Shannon sampling theorem. We replace all the odd columns of the full sampling pattern with the corresponding columns of the full sampling pattern for the inner region (Fig. 4c); this still satisfies the requirements of the Nyquist-Shannon sampling theorem for the inner region.

Figure 4c shows the proposed sampling pattern for the non-rectangular FOV; the gray dots are those that were used to reconstruct the outer image; the blue dots are the sample locations that will be added for the inner image. The samples added into the pattern to reconstruct the inner image are positioned horizontally at the odd columns of the original fully-sampled pattern, but are separated by the inverse of the vertical extent of the inner region. The increased vertical separation between samples is the reason why the new sampling pattern has a reduced number of samples when compared to the original full sampling pattern. Note that this sampling pattern is not generally a lattice; it is not simply a replication of a basic pattern. Instead, it is the union of two Cartesian sampling patterns.

3.2. **Image reconstruction.** In this subsection, we will first describe the direct (non-iterative) approach. We will then discuss an iterative model-based approach where the reconstructed image is the solution of an optimization problem [21].

3.2.1. *Direct reconstruction.* Let I, I_{outer}, and I_{inner} denote the image, the outer region, and the inner region, respectively. Let F denote the DFT, let $\mathcal{F}$ denote the continuous Fourier transform, and let $F_{nu}^{(k)}$ denote the non-uniform DFT to the set of frequencies contained in the set k. The I_{outer} image is reconstructed from the even columns of the sampling pattern. Then

$$\begin{aligned} \mathcal{F}(I) &= \mathcal{F}\left(I_{\text{outer}}\right) + \mathcal{F}\left(I_{\text{inner}}\right) \\ \Rightarrow I_{\text{inner}} &= \mathcal{F}^{-1}\left\{\mathcal{F}(I) - \mathcal{F}\left(I_{\text{outer}}\right)\right\}. \end{aligned} \tag{2}$$

Equation (2) amounts to the reconstruction algorithm for I_{inner}, where the continuous Fourier transforms are replaced by the appropriate DFT [22] (either gridding [24, 5, 18] or inverse gridding [37, 41]) . Let $F_{nu}^{(k)}$ and $F_{nu}^{\text{inv},(k)}$ denote gridding and inverse gridding, respectively[2].

Let k_{even} and k_{odd} denote the set of frequencies collected from the even and odd columns of the sampling pattern, respectively. Let $k_{\text{all}} = k_{\text{odd}} \cup k_{\text{even}}$. Let k_{inner} denote the set of frequencies that would be required for a fully-sampled pattern of the inner region (Fig. 4b). Let $\mathcal{F}\{I\}_{\text{even}}$, $\mathcal{F}\{I\}_{\text{odd}}$, and $\mathcal{F}\{I\}_{\text{all}}$ denote $\mathcal{F}\{I\}(k_{\text{even}})$, $\mathcal{F}\{I\}(k_{\text{odd}})$, and $\mathcal{F}\{I\}(k_{\text{all}})$, respectively. Let S denote a 2D array of the size of the image with values of 1 for those pixels within the non-rectangular FOV, and 0 otherwise. Let S_{outer} and S_{inner} denote 2D arrays that indicate the outer and inner images, respectively. The direct (non-iterative) algorithm for reconstruction of an image with a non-rectangular FOV is presented in Alg. 1. This algorithm does the following: 1) reconstructs the outer region from the even columns, 2) interpolates all data onto the fully-sampled pattern for the inner region, 3) subtracts the Fourier values of the outer region from the samples of the inner grid, 4) reconstructs the inner region, and 5) sums the outer and inner regions together to create the final image.

Algorithm 1: Direct reconstruction with a non-rectangular FOV

```
**Inputs:** $S$, $k_{\text{even}}$, $k_{\text{odd}}$, $\mathcal{F}\{I\}_{\text{even}}$, and $\mathcal{F}\{I\}_{\text{odd}}$
$I_{\text{even}} = F^{-1}\left(\mathcal{F}\{I\}_{\text{even}}\right)$
$I_{\text{outer}} = S_{\text{outer}} \odot I_{\text{even}}$
$F_{\text{inner,even}} = F_{nu}^{\text{inv},(k_{\text{inner}})}\left(I_{\text{even}}\right)$
$F_{\text{inner}} = \mathcal{F}\{I\}_{\text{odd}} \cup F_{\text{inner,even}}$
$I_{\text{inner}} = F_{nu}^{(k_{\text{inner}})}\left[F_{\text{inner}} - F_{nu}^{\text{inv},(k_{\text{inner}})}\left(I_{\text{outer}}\right)\right]$
$I = S \odot \left(I_{\text{inner}} + I_{\text{outer}}\right)$
**Output:** $I$
```

---

[2] Note that, in general, F_{nu} is not invertible and F_{nu}^{inv} is an approximation to its inverse.

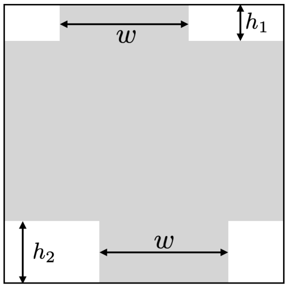

FIGURE 5. The shape of the largest connected object that can be reconstructed accurately with the method described. Note that the two lengths labeled w must be equal; however, the lengths labeled h_1 and h_2 need not be.

With parallel MRI, where multiple coils simultaneously collect data at the same spatial frequencies, we can also use the direct algorithm. To do so, we will determine the non-rectangular FOV for each sensitized image $\sigma^{(j)} I$; here, $\sigma^{(j)}$ denotes the sensitivity of the j^{th} coil. A simple approach would be to compute the union of these non-rectangular FOVs, and proceed to reconstruct each coil's image using Alg. 1. Alternatively, one could use the PISCO algorithm to automatically determine a non-rectangular FOV [29]. However, this would yield a sampling pattern that is likely to be more burdensome than is necessary. Instead, we will individually identify each coil's non-rectangular FOV, determine the resulting sampling pattern for each individual non-rectangular FOV, and use the resulting sampling pattern with the most number of samples. The image for each coil $I^{(j)}$ is reconstructed using Alg. 1. Then, each coil's image is multiplied by the support for that coil: $I^{(j)} := S^{(j)} \odot I^{(j)}$. The images from all coils can then be combined into a single image using the method of Roemer et al. [42].

For the sampling pattern described with the direct reconstruction method presented, the non-rectangular FOV is not generally a convex set. The shape and maximum size that the object could be is indicated in Fig. 5.

3.2.2. *Model-based reconstruction.* With Fourier sensing, one can reconstruct the image by solving the following optimization problem: minimize $\|F_{nu}\, I - b\|$, where $\|\cdot\|$ represents a norm, b represents the data collected, and I is the optimization variable. When Gaussian noise is present, which is what we will assume for the remainder of this manuscript, the solution that minimizes the ℓ_2 norm is the maximum likelihood estimate (MLE). For the special case where the data collected is on a Cartesian grid centered on the 0 frequency and satisfies the Nyquist-Shannon sampling theorem, $F_{nu} = F$ and the MLE reconstruction is $I^\star = F^{-1} b$.

When a non-rectangular FOV is provided with a corresponding support S, one can find the MLE by solving

$$\text{minimize } \|F_{nu}\, I - b\|_2 \text{ subject to } S^C \odot I = 0.$$

Here, $S^C = 1 - S$ indicates pixels that lie outside the non-rectangular FOV. For the case where the data is collected on a Cartesian grid, this problem becomes

$$\text{minimize } \|M_b\, F\, I - b\|_2 \text{ subject to } S^C \odot I = 0,$$

where M_b is a mask that indicates which data values of the Cartesian grid were collected.

In [43], Samsonov et al. suggest using the Projection Onto Convex Sets (POCS) algorithm to solve this problem. This approach iterates over the following two steps: 1) project onto the set of images that are consistent with the data collected, and 2) project onto the set of images where pixels outside of the FOV all have values equal to 0. While effective, this algorithm is slow to converge. It is also intuitively inefficient: we should not need to include pixels outside of the FOV in the optimization variable if we know their values are all 0. Instead, we propose solving the following optimization problem:

$$\text{minimize} \;\; \| F_{nu} \, M_S^T \, \tilde{I} - b \|_2. \tag{3}$$

Here, $\tilde{I}$ is a vector of those pixels within the FOV and M_S is the linear transformation such that $M_S I$ is a vector of only those elements of I that are within the FOV. If the data lies on a Cartesian grid, F_{nu} can be replaced with $M_b \, F$. Note that this is a special case of the problem formulation presented in [38].

Problem (3) is a least-squares problem; it can either be solved analytically using the pseudo-inverse [47], or it can be solved numerically with LSQR [35], which converges to a solution much faster than POCS.

We extend the formulation of (3) to the case of parallel MRI as follows:

$$\text{minimize} \;\; \| \boldsymbol{F_{nu}} \, \boldsymbol{\sigma} \, M_S^T \, \tilde{I} - \boldsymbol{b} \|_2, \tag{4}$$

where $\boldsymbol{\sigma} = \left[\sigma^{(1)}, \sigma^{(2)}, \ldots, \sigma^{(C)} \right]^T$, $\sigma^{(j)}$ is a diagonal matrix for the j^{th} coil with diagonal elements equal to its sensitivity values, C is the number of coils used for data collection, $\boldsymbol{F_{nu}}$ is a block-diagonal matrix where each block is F_{nu}, $\boldsymbol{b} = [b^{(1)}, b^{(2)}, \ldots, b^{(C)}]^T$, and $b^{(j)}$ is a vector of data collected by the j^{th} coil. Problem (4) can also be solved with LSQR [35]. Note that the additional information provided by the multiple coils can reduce the number of samples required for a high-quality image [14].

Problems (3) and (4) need not use the sampling pattern described in this manuscript. These problems can be solved for any sampling pattern (e.g., spiral [2, 32] or rosette [34, 10]).

4. Experiments.

Section 5 will present results of experiments involving MRI data of a sagittal slice of an ankle, an axial slice of a pineapple, and axial slices of a brain. For all of the data presented, the data was collected with two dimensions of phase-encodes and one dimension of readout. The data was then inverse Fourier transformed along the readout direction to place the data into the (k_x, k_y, z) hybrid domain [4] (where x, y, z are the spatial coordinates and k_x, k_y, k_z are the frequency coordinates). Once in the hybrid domain, the slice of each z location is reconstructed independently. Each dataset was normalized so that the maximum Fourier value had a magnitude of 1.

MRI Data of the pineapple and brain were collected with a 3 Tesla clinical MRI machine for the purposes of the research presented in this manuscript. These data were collected with currently available clinical scanning protocols by combining alternating columns from two separate acquisitions with different FOVs. Any subject motion that occurs in between data collections leads to errors in the reconstruction. All procedures performed in studies involving human participants were in accordance with the ethical standards of the institutional and/or national research

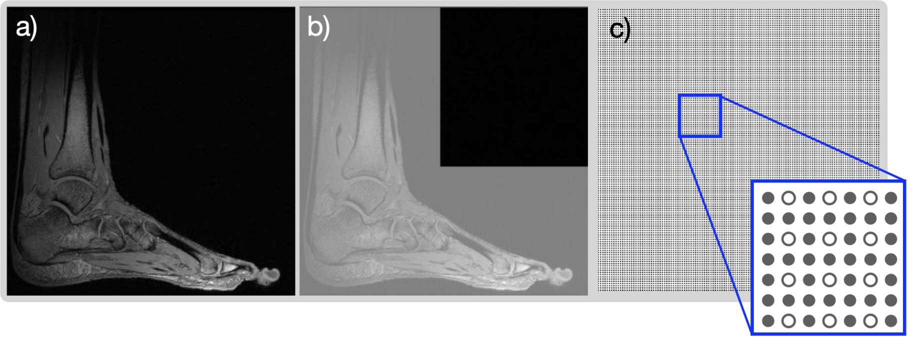

FIGURE 6. Subfigure (a) shows a sagittal slice of an ankle and foot; (b) shows a corresponding non-rectangular FOV that does not include the upper-right quadrant, and (c) shows the corresponding sampling pattern for the non-rectangular FOV of (b). The sampling burden of the reduced sampling pattern is 75%.

committee and with the 1964 Helsinki declaration and its later amendments or comparable ethical standards. Data were collected with health insurance portability and accountability act (HIPPA) compliance and we obtained prospective informed consent from the volunteer under COMIRB #19-0158.

The data of the ankle was collected with a 3D Cartesian full sampling pattern with two dimensions of phase-encodes and one dimension of readout (Fig. 6). The data was collected using a 3 Tesla clinical MRI machine with a dedicated ankle coil array and was shared publicly as part of [15]. For the ankle, we will first simulate a single-coil acquisition: we will reconstruct the image from the fully-sampled data for all coils and we will combine those images using the method of [42]. This will be considered the *true* image. We will Fourier transform this image to generate the data of the full sampling pattern, and we will eliminate 25% of the data according to the sampling pattern of Fig. 6c for reconstruction with the non-rectangular FOV of Fig. 6b. Separately, we will perform a parallel MRI reconstruction where we will simulate the data that would have been acquired with the reduced sampling pattern. To do so, we will first reconstruct the image of each coil from the fully-sampled data; we will then use inverse gridding to estimate the Fourier values for the spatial frequencies of the reduced sampling pattern.

The data of the pineapple and the brain were collected using a 3 Tesla clinical MRI machine with a birdcage coil array. For these datasets, both a fully-sampled 3D Cartesian dataset and a prospectively undersampled dataset with the sampling pattern described for a non-rectangular FOV were collected.

Initially, for the ankle, we will use a non-rectangular FOV that consists of the 2nd, 3rd, and 4th quadrants. That is, the FOV will not include the 1st quadrant, as depicted in Fig. 6b. For this FOV, the sampling pattern consists of every other row and every other column of the fully-sampled pattern; that is, in every 2×2 block of samples three samples are included in the sampling pattern, as shown in Fig. 6c. This will allow us to compare the results with *retrospective downsampling.* That is, we will reconstruct the image from the fully-sampled pattern and then reconstruct the image using only the samples from the sampling pattern of Fig. 6c. Though

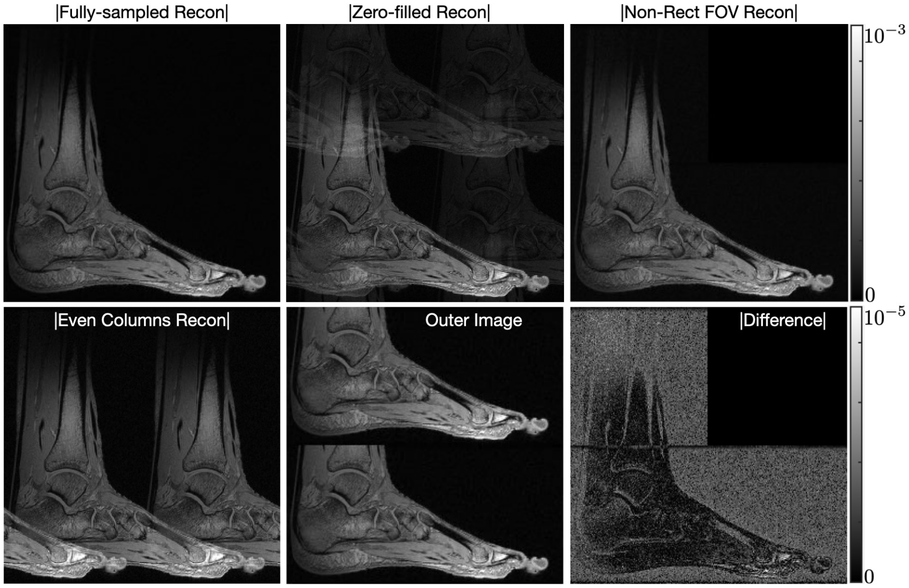

Figure 7. Magnitude image reconstructions of a sagittal slice of an ankle and foot: a) shows the fully-sampled reconstruction, b) shows the zero-filled reconstruction with the non-rectangular FOV sampling pattern of Fig. 6b with a sampling burden of 75%, c) shows the reconstruction using Alg. 1, c) the reconstruction using only the even columns of data, d) the reconstruction after subtracting away the Fourier values of the inner region, and e) the difference between (a) and (c).

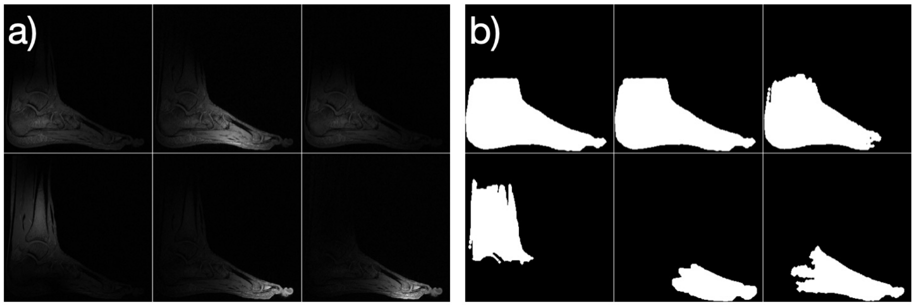

Figure 8. Image reconstructions for six coils of a dedicated ankle array - a) Magnitude images for each coil, and b) the non-rectangular FOV determined using the intensity images of (a).

the sampling pattern presented in this manuscript is not generally a lattice, for this case, the sampling pattern is a lattice (as shown in Fig. 6c).

5. **Results.** For the following results, let the *sampling burden* be the ratio of the number of samples of the given pattern to the number of samples of the full sampling pattern. When coil sensitivities were required, they were estimated with

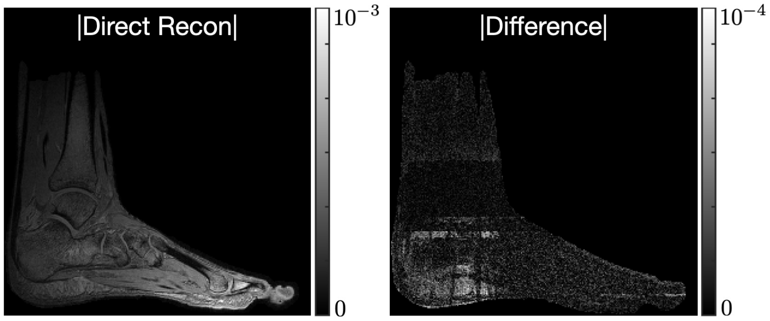

FIGURE 9. Magnitude image reconstruction of the ankle using the direct reconstruction methods and the sampling pattern determined according to the individual coil FOVs shown in Fig. 8b with a sampling burden of 63%. The difference image shows the type of the errors that arise from this method; these errors are due to the fact that individual coils sense the whole subject imaged.

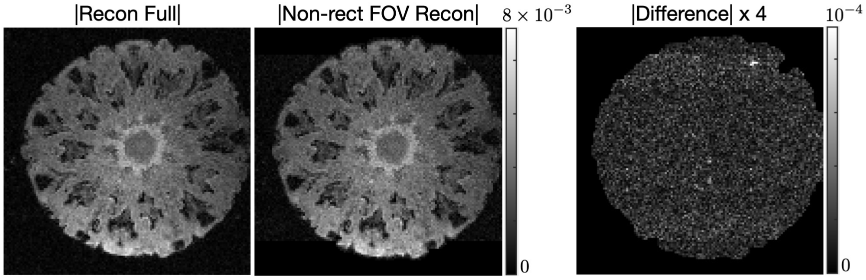

FIGURE 10. Magnitude image reconstructions of an axial slice of a pineapple from data collected with a single coil: left) the fully sampled reconstruction, center) the direct reconstruction from the undersampled pattern with a burden of 87.5%, and right) the scaled magnitude of the difference.

fully-sampled data using the method of Pruessman et al. [40].

Figure 7 shows the direct reconstruction for the ankle from the simulated single-coil acquisition. The magnitude of the difference ranges up to 10^{-5}. The sampling pattern for the non-rectangular FOV has a burden of 75%.

Figure 8 shows the individual coil images from six coils of the ankle array and the corresponding supports of each image determined by their signal intensity. The sampling pattern determined using these supports, as described in Sec. 3, has a sampling burden of 63%.

Figure 9 shows the reconstruction along with its difference from the fully-sampled reconstruction. This reconstruction was accomplished with a sampling burden of 53%. The difference with the fully-sampled reconstruction ranges up to 10^{-4}. The larger errors are due to the assumption of the smaller supports. In truth, each coil senses the entire ankle, which leads to the errors in the results.

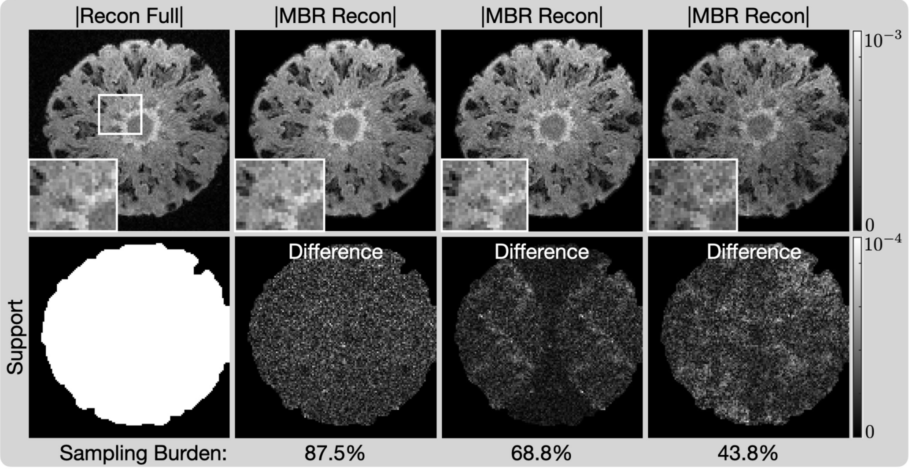

FIGURE 11. Model-based magnitude image reconstructions of an axial slice of a pineapple with sampling burdens of (from left to right) 100%, 87.5%, 68.8%, and 43.8%.

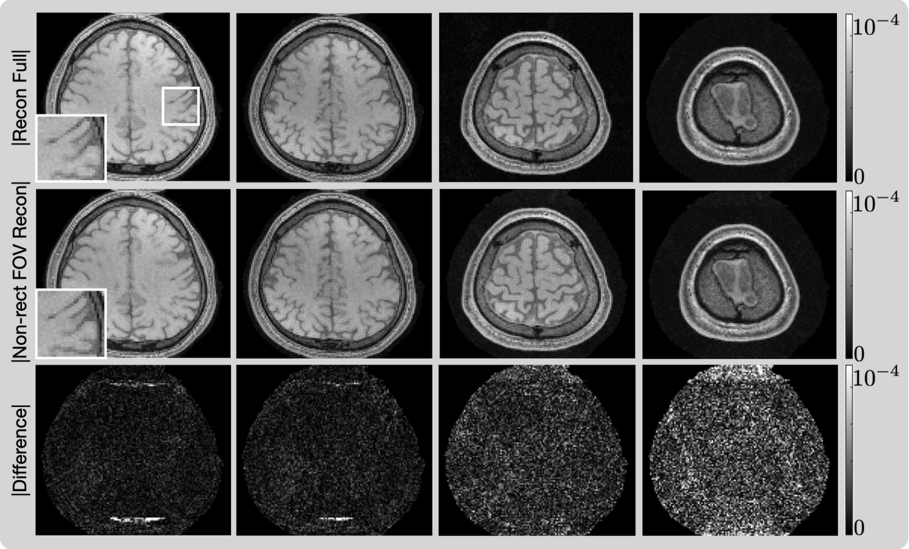

FIGURE 12. Magnitude image reconstructions using the direct method for four axial slices of a brain using data collected with an 8 coil array. The sampling pattern of the non-rectangular FOV had a burden of 95%.

Figure 10 shows the direct reconstruction with a single coil for an axial slice of a pineapple. The non-rectangular FOV was accomplished with an 87.5% sampling burden.

Figure 11 shows the model-based reconstruction of the axial slice of a pineapple with data collected from a 14 coil array. Results are presented with sampling burdens of 87.5%, 68.8%, and 43.8%. The sampling pattern was reduced by eliminating alternating samples from the even columns, and then eliminating alternating samples from the odd columns. The mean squared error of the undersampled reconstructions are 1.6×10^{-9}, 3.0×10^{-9}, and 7.1×10^{-9}, respectively.

Figure 12 shows reconstructions using the non-rectangular FOV and compares them to the fully-sampled reconstructions for several slices of a human brain. The sampling pattern of the non-rectangular FOV had a 95% sampling burden. The differences for all slices range from 0 to 10^{-4}. As in all other examples, taking advantage of the non-rectangular FOV reconstructs a high-quality image with a reduced sampling burden. The significant errors in the reconstruction are due to subject motion in between the full sampling pattern and the reduced sampling pattern; this would largely be eliminated if data were collected during a single scanning protocol.

6. Conclusion.

The method presented in this manuscript takes advantage of a non-rectangular FOV with Fourier sensing to reconstruct a high-quality image with fewer samples. This FOV need not be convex nor connected. We presented both a direct method of reconstruction as well as an iterative method for reconstruction. Note that Gridding and inverse Gridding both take advantage of the Fast Fourier transform and are $\mathcal{O}(n \log n)$ algorithms (where n is the number of elements of the input). Since the direct reconstruction algorithm takes advantage of Gridding and Inverse Gridding, it too has a computational complexity of $\mathcal{O}(n \log n)$. Note that the signal-to-noise (SNR) ratio may be dependent on the amount of data collected; therefore, reducing the amount of data collected may have an adverse affect on image quality. For example, the SNR of MRI depends on the length of time spent collecting data [33]. Therefore, taking advantage of the reduced sampling burden would reduce the SNR correspondingly, which may reduce overall image quality. This would be especially relevant for low-field MRI, for example, where the SNR is a limiting factor in image quality [44, 26].

The presented method reconstructs the image accurately as long as the non-rectangular FOV is a superset of the object's support. Pixels within the FOV may be absent of any object. However, to avoid errors, all pixels exterior to the FOV must be absent of any object.

In this manuscript, we also presented an iterative method of reconstructing an image with a non-rectangular FOV. By incorporating this FOV into the objective function, we were able to eliminate the need for a projection operator and use a more efficient numerical solver than previous methods. We further showed that we could reconstruct a high-quality image with even fewer samples in the parallel MRI setting.

Regularization terms can be added into the objective functions of (3) and (4), which could allow for high-quality reconstructions with even fewer samples. Thus, one could incorporate compressed sensing [11, 31], perhaps with structured sparsity [17, 16], into the reconstruction. E.g., the sampling pattern could be a variable density subset of that proposed in this manuscript, and the image could be reconstructed by solving the following optimization problem:

$$\text{minimize} \;\; \| \boldsymbol{F_{nu}} \, \boldsymbol{\sigma} \, M_S^T \, \tilde{I} - \boldsymbol{b} \|_2 + \lambda \| \Psi \, \tilde{I} \|_1, \tag{5}$$

where Ψ is a sparsifying transformation, and the ℓ_1 norm $\| \cdot \|_1$ encourages sparsity. Incorporating the additional knowledge of the known support into a compressed sensing reconstruction should yield a higher-quality reconstruction for the same number of samples. We will pursue this approach in future work.

Alternatively, problem (5) assumes that the values for those pixels outside of the support are exactly equal to 0. Due to noise (largely due to thermal Brownian motion in MRI [20]), the values of those pixels outside of the support will be small but non-zero. In future work, we will alter the optimization problem as follows:

$$\text{minimize } \|\boldsymbol{F_{nu}}\,\boldsymbol{\sigma}\,I - \boldsymbol{b}\|_2 + \lambda\|\Psi\,\tilde{I}\|_1 \text{ subject to } \|M_{\bar{S}}I\|_2 \leq \epsilon,$$

where $M_{\bar{S}}$ is a matrix that isolates those pixels outside of the support into a vector (the $\bar{\cdot}$ indicates the complement set), and ϵ is a noise bound (which can be identified from an MRI scan without any excitation). An equivalent form of this problem can be solved with the Fast Iterative Shrinkage Threshold Algorithm [6].

Note that once the Fourier values of the inner region are estimated at the spatial frequencies in k_{inner}, the data lies on a Cartesian grid. This indicates that, rather than using gridding to reconstruct I_{inner}, one could instead use the inverse DFT, which would be more efficient.

In this work, we assumed that the even columns would be the alternating columns of a full sampling pattern. This led to aliasing by half the FOV as depicted in Fig. 3a. Alternatively, one could permit an arbitrary amount of aliasing, which would correspond to different separations between the even columns. By searching over the amount of aliasing, it is likely that one would find a sampling pattern with fewer samples than that presented in this manuscript. In the same vein, one could try to identify a rotation of the sampling pattern that leads to a reduced sampling burden. Referring to Fig. 5, if the object had substance in the corners but was vacant near the edges but away from the corners, then a rotation of the FOV would lead to a reduced sampling pattern. We leave this pursuit as future work.

MATLAB code for reconstructing images in accordance to the methods of this manuscript will be made available at `https://github.com/ndwork/nonRectSupport` and at www.nicholasdwork.com. The pineapple and brain data collected for this manuscript will also be made publicly available at www.nicholasdwork.com.

Acknowledgments. This work was supported by the University of Colorado through a research grant awarded by the Anschutz-Boulder Nexus (AB Nexus) Initiative. EE is supported by an award from the American Heart Association 853697 and NIH/NCATS Colorado CTSA Grant Number K12 TR004412 and UM1 TR004399. Contents are the authors' sole responsibility and do not necessarily represent official NIH views.

REFERENCES

[1] N. Aggarwal and Y. Bresler, Patient-adapted reconstruction and acquisition dynamic imaging method (PARADIGM) for MRI, *Inverse Problems*, **24** (2008), 045015, 29 pp.

[2] C. B. H. Ahn, J. Kim and Z. H. Cho, High-speed spiral-scan echo planar NMR imaging-I, *IEEE Transactions on Medical Imaging*, **5** (1986), 2-7.

[3] C. A. Baron, N. Dwork, J. M. Pauly and D. G. Nishimura, Rapid compressed sensing reconstruction of 3D non-cartesian MRI, *Magnetic Resonance in Medicine*, **79** (2018), 2685-2692.

[4] P. Beatty, A. Brau, S. Chang, S. Joshi, C. Michelich, E. Bayram, T. Nelson, R. Herfkens and J. Brittain, A method for autocalibrating 2D accelerated volumetric parallel imaging with clinically practical reconstruction times, in *Proceedings of the International Society for Magnetic Resonance in Medicine*, vol. 15, 2007, 1749.

[5] P. J. Beatty, D. G. Nishimura and J. M. Pauly, Rapid gridding reconstruction with a minimal oversampling ratio, *IEEE Transactions on Medical Imaging*, **24** (2005), 799-808.

[6] A. Beck and M. Teboulle, A fast iterative shrinkage-thresholding algorithm for linear inverse problems, *SIAM Journal on Imaging Sciences*, **2** (2009), 183-202.

[7] J. B. Birdsong and N. I. Rummelt, The hexagonal fast fourier transform, in *IEEE International Conference on Image Processing (ICIP)*, IEEE, (2016), 1809-1812.

[8] R. N. Bracewell, Radio astronomy techniques, in *Astrophysics V*, Springer, 1962, 42-129.

[9] R. N. Bracewell, *Two-Dimensional Imaging*, Prentice-Hall, Inc., 1995.

[10] A. M. Bush, C. M. Sandino, S. Ramachandran, F. Ong, N. Dwork, E. J. Zucker, A. B. Syed, J. M. Pauly, M. T. Alley and S. S. Vasanawala, Rosette trajectories enable ungated, motion-robust, simultaneous cardiac and liver t2* iron assessment, *Journal of Magnetic Resonance Imaging*, **52** (2020), 1688-1698.

[11] E. J. Candès and M. B. Wakin, An introduction to compressive sampling, *IEEE Signal Processing Magazine*, **25** (2008), 21-30.

[12] K. F. Cheung and R. J. Marks, Imaging sampling below the nyquist density without aliasing, *Journal of the Optical Society of America A*, **7** (1990), 92-105.

[13] E. K. Cole, F. Ong, S. S. Vasanawala and J. M. Pauly, Fast unsupervised MRI reconstruction without fully-sampled ground truth data using generative adversarial networks, in *Proceedings of the IEEE/CVF International Conference on Computer Vision*, 2021, 3988-3997.

[14] A. Deshmane, V. Gulani, M. A. Griswold and N. Seiberlich, Parallel MR imaging, *Journal of Magnetic Resonance Imaging*, **36** (2012), 55-72.

[15] N. Dwork, J. W. Gordon and E. K. Englund, Accelerated parallel magnetic resonance imaging with compressed sensing using structured sparsity, *Journal of Medical Imaging*, **11** (2024), 033504.

[16] N. Dwork and P. E. Larson, Utilizing the structure of a redundant dictionary comprised of wavelets and curvelets with compressed sensing, *Journal of Electronic Imaging*, **31** (2022), 063043.

[17] N. Dwork, D. O'Connor, C. A. Baron, E. M. I. Johnson, A. B. Kerr, J. M. Pauly and P. E. Z. Larson, Utilizing the wavelet transform's structure in compressed sensing, *Signal, Image and Video Processing*, **15** (2021), 1407-1414.

[18] N. Dwork, D. O'Connor, E. M. I. Johnson, C. A. Baron, J. W. Gordon, J. M. Pauly and P. E. Z. Larson, Optimization in the space domain for density compensation with the nonuniform FFT, *Magnetic Resonance Imaging*, **100** (2023), 102-111.

[19] D. E. Dudgeon, *Multidimensional Digital Signal Processing*, Prentice-hall, 1983.

[20] R. R. Ernst, G. Bodenhausen and A. Wokaun, *Principles of Nuclear Magnetic Resonance in One and Two Dimensions*, Oxford university press, 1990.

[21] J. A. Fessler, Model-based image reconstruction for MRI, *IEEE Signal Processing Magazine*, **27** (2010), 81-89.

[22] L. Greengard and J.-Y. Lee, Accelerating the nonuniform fast fourier transform, *SIAM Review*, **46** (2004), 443-454.

[23] J. P. Haldar, Low-rank modeling of local k-space neighborhoods (loraks) for constrained MRI, *IEEE Transactions on Medical Imaging*, **33** (2013), 668-681.

[24] J. I. Jackson, C. H. Meyer, D. G. Nishimura and A. Macovski, Selection of a convolution function for fourier inversion using gridding (computerised tomography application), *IEEE Transactions on Medical Imaging*, **10** (1991), 473-478.

[25] H. Kajbaf, J. T. Case, Z. Yang and Y. R. Zheng, Compressed sensing for sar-based wideband three-dimensional microwave imaging system using non-uniform fast fourier transform, *IET Radar, Sonar & Navigation*, **7** (2013), 658-670.

[26] W. T. Kimberly, A. J. Sorby-Adams, A. G. Webb, E. X. Wu, R. Beekman, R. Bowry, S. J. Schiff, A. de Havenon, F. X. Shen, G. Sze, et al., Brain imaging with portable low-field MRI, *Nature Reviews Bioengineering*, **1** (2023), 617-630.

[27] P. E. Z. Larson, M. S. Lustig and D. G. Nishimura, Anisotropic field-of-view shapes for improved PROPELLER imaging, *Magnetic Resonance Imaging*, **27** (2009), 470-479.

[28] Z.-P. Liang, Constrained reconstruction methods in mr imaging, *Rev. Magn. Reson. Med.*, **4** (1992), 67.

[29] R. A. Lobos, C.-C. Chan and J. P. Haldar, New theory and faster computations for subspace-based sensitivity map estimation in multichannel MRI, *IEEE Transactions on Medical Imaging*, **43** (2023), 286-296.

[30] Y. M. Lu, M. N. Do and R. S. Laugesen, A computable fourier condition generating alias-free sampling lattices, *IEEE Transactions on Signal Processing*, **57** (2009), 1768-1782.

[31] M. Lustig, D. Donoho and J. M. Pauly, Sparse MRI: The application of compressed sensing for rapid MR imaging, *Magnetic Resonance in Medicine*, **58** (2007), 1182-1195.

[32] C. H. Meyer, B. S. Hu, D. G. Nishimura and A. Macovski, Fast spiral coronary artery imaging, *Magnetic Resonance in Medicine*, **28** (1992), 202-213.

[33] D. G. Nishimura, *Principles of Magnetic Resonance Imaging*, lulu.com, 1996.

[34] D. C. Noll, Multishot rosette trajectories for spectrally selective MR imaging, *IEEE Transactions on Medical Imaging*, **16** (1997), 372-377.

[35] C. C. Paige and M. A. Saunders, LSQR: An algorithm for sparse linear equations and sparse least squares, *ACM Transactions on Mathematical Software (TOMS)*, **8** (1982), 43-71.

[36] A. Papoulis, *Signal Analysis*, Mcgraw-Hill, 1977.

[37] J. Pauly, Non-Cartesian reconstruction, 2005.

[38] X. Peng, H.-Q. Du, F. Lam, S. D. Babacan and Z.-P. Liang, Reference-driven MR image reconstruction with sparsity and support constraints, in *2011 IEEE International Symposium on Biomedical Imaging: From Nano to Macro*, IEEE, 2011, 89-92.

[39] S. K. Plevritis and A. Macovski, Spectral extrapolation of spatially bounded images, *IEEE Transactions on Medical Imaging*, **14** (1995), 487-497.

[40] K. P. Pruessmann, M. Weiger, M. B. Scheidegger and P. Boesiger, SENSE: Sensitivity encoding for fast MRI, *Magnetic Resonance in Medicine*, **42** (1999), 952-962.

[41] V. Rasche, R. Proksa, R. Sinkus, P. Bornert and H. Eggers, Resampling of data between arbitrary grids using convolution interpolation, *IEEE Transactions on Medical Imaging*, **18** (1999), 385-392.

[42] P. B. Roemer, W. A. Edelstein, C. E. Hayes, S. P. Souza and O. M. Mueller, The NMR phased array, *Magnetic Resonance in Medicine*, **16** (1990), 192-225.

[43] A. A. Samsonov, E. G. Kholmovski, D. L. Parker and C. R. Johnson, POCSENSE: POCS-based reconstruction for sensitivity encoded magnetic resonance imaging, *Magnetic Resonance in Medicine*, **52** (2004), 1397-1406.

[44] M. Sarracanie, C. D. LaPierre, N. Salameh, D. E. Waddington, T. Witzel and M. S. Rosen, Low-cost high-performance MRI, *Scientific Reports*, **5** (2015), 15177.

[45] K. Scheffler and J. Hennig, Reduced circular field-of-view imaging, *Magnetic Resonance in Medicine*, **40** (1998), 474-480.

[46] T. J. Sumpf, M. Uecker, S. Boretius and J. Frahm, Model-based nonlinear inverse reconstruction for T2 mapping using highly undersampled spin-echo MRI, *Journal of Magnetic Resonance Imaging*, **34** (2011), 420-428.

[47] L. N. Trefethen and D. Bau, *Numerical Linear Algebra*, SIAM, 1997.

[48] Y. Wang and W. Yin, Sparse signal reconstruction via iterative support detection, *SIAM Journal on Imaging Sciences*, **3** (2010), 462-491.

[49] Z. Yaqoob, J. Wu and C. Yang, Spectral domain optical coherence tomography: A better OCT imaging strategy, *Biotechniques*, **39** (2005), S6-S13.

Received November 2024; revised March 2025.